

CdS Nanocrystals Entrapped in Thin SiO₂ Films

M. T. Pham,* D. Möller, W. Matz, and A. Mücklich

Forschungszentrum Rossendorf e.V., Institut für Ionenstrahlphysik und Materialforschung, Postfach 51 01 19, D-01314 Dresden, Germany

S. Oswald

Institut für Festkörperphysik und Werkstofforschung, Postfach 01171, Helmholtzstrasse 20, D-01069 Dresden, Germany

Received: September 18, 1997; In Final Form: February 10, 1998

Thin films of SiO₂ entrapping CdS nanocrystals were prepared by implanting Cd⁺ and S⁺ ions into a planar 100 nm thin SiO₂ film structure. CdS crystallite formation was shown to be the result of the oxidation of the preformed Cd nanoparticles by energetic S⁺ ions. The subsequent annealing led to completing the process toward CdS and removal of unreacted Cd and S from the film and contributed to a narrowing in particle size distribution. CdS nanocrystals obtained are of hexagonal structure and nearly spherically shaped with an average size of 7 nm.

Introduction

Nanocrystallite quantum dots (QD) of II–VI semiconductor materials are synthesized commonly by wet chemical methods.^{1–5} For use in practical zero-dimensional devices, e.g., optical switches or modulators, an immobilization of quantum dots in a condensed phase is the approach of choice. A variety of technologies have been developed for manufacturing QD incorporated in solid materials^{6–9} or bound to metal surfaces.¹⁰ In view of integrating into existing microelectronic architectures, an adequate synthetic route is of interest. This paper describes the synthesis of CdS nanocrystals and their in situ incorporation into a thin SiO₂ film on common silicon planar structures, using ion implantation. The technique has been used by Ekimov et al. for preparing CdSe.¹¹ The procedure involves sequential implantation of the constituent components Cd and S into the matrix followed by a thermal treatment. Implantation to produce CdS nanocrystals within a solid surface differs from the synthetic routes above in some respects. In the standard process the heavy Cd will be implanted before S to facilitate the production of predictable concentration profiles of incident species. Previous research has shown that high dose implantation of metal into dielectric films results generally in metallic nanoparticles.¹² The nucleation and growth of CdS will result thus from the reaction of matrix-embedded Cd nanoparticles with a beam of energetic S ions/atoms. The second point refers to how the target product is purified from byproducts. Furthermore, the new phase nucleates and grows inside a solid matrix which necessarily confers some template effects associated with the reduced mobility and spatial confinement.

In the present paper we studied the effect of the subsequent annealing on the formation of CdS from the Cd–S–SiO₂ system generated by ion implantation. The ion dose and energy are fixed to produce a concentration level at the profile maximum of 2.9×10^{22} Cd/cm³ (sufficient for nucleation during implantation) inside a 100 nm SiO₂ film. The quantum dots and film structure are characterized using X-ray photoelectron spectroscopy, X-ray diffraction, and transmission electron microscopy.

Experiment

Substrates used for ion implantation were multilayer thin film structures, prepared on Si wafers using standard semiconductor technologies: 100 nm SiO₂/100 nm Si₃N₄/70 nm SiO₂/p-Si. Cd and S ions were sequentially implanted into the topmost layer of SiO₂. The depth distribution of Cd and S implanted into SiO₂ was simulated by TRIM code¹³ and profile code¹⁴ to get an approximately overlapping concentration profiles for Cd and S. The result yielded the selection of ion dose and energy of 8×10^{16} ions/cm² at 100 keV for Cd and 5×10^{16} ions/cm² at 17 keV for S. Implantation was made at normal incidence angle (relative to the surface) without substrate cooling. The annealing following implantation was conducted at varying temperatures (from 500 to 800 °C) for 10 min and 3 h in a nitrogen ambient.

Morphology and metrics of nanoparticles in the implanted samples were studied using a transmission electron microscope (Philips CM300) operated at 300 kV with point resolution of 2.0 Å. Images were collected in bright field with an objective aperture selected to permit lattice imaging of CdS, CdO, Cd, and S. Cross sections of the implanted samples were used.

X-ray diffraction (XRD) measurements were carried out on a step scan diffractometer (URD-6) in grazing incidence geometry $\omega = 1^\circ$ using a thin film attachment with Cu K α radiation. The counting time per step and the step size were 15–30 s and 0.1°, respectively. Samples as-prepared were used directly in XRD measurements without any further treatment.

X-ray photoelectron spectroscopy (XPS) spectra were collected on a Physical Electronic 5600 ESCA with monochromated Al K α X-ray source operated at 350 W. The X-ray angle and electron exit angle were 45° relative to the sample surface. The emitted photoelectrons were collected from an area of 800 μ m diameter. Angle-dependent spectra were obtained by varying the angle between the plane of the sample surface and the axis of the detector. Measurements were made at takeoff angles of 75°, 45°, and 15° which correspond to increasing surface sensitivity. High-resolution narrow-scan spectra were measured for the core levels of Cd 3d, S 2s, S 2p, and O 1s. Reference to C 1s, Si 2p, and O 1s (from SiO₂ substrate) was

used to account for specimen charging. The depth profiling was obtained by sputtering with a 3.5 keV Ar ion gun at a current density of about $70 \mu\text{A}/\text{cm}^2$, corresponding to a sputter rate of 3 nm at Ta_2O_5 . For depth profiling measurements the nonmonochromatized Al K α source (400 W) was used, which led to a minimizing of the surface charging up due to electrons from the X-ray source.

Results and Discussion

Electron Microscopic Characterization. TEM images in cross-sectional view ($200\times$ magnification) are shown in Figure 1 of samples subjected to a systematic annealing. Part (a) stands for as-implanted Cd. From (b) to (f) the results are presented for the co-implantation of Cd and S before and after annealing (10 min in nitrogen atmosphere) at 500, 600, 700, and 800 °C, respectively. In all samples, the implanted layer is seen to be confined inside the topmost SiO_2 film. With reference to the known thickness of the underlying layers Si_3N_4 (100 nm) and SiO_2 (70 nm), changes in thickness of the implanted layer due to implantation and annealing can be derived. The results are listed in Table 1. The thickness loss after the Cd implantation is roughly 20%. The subsequent S implantation results in a further loss of about 5%. This result is expected due to sputtering induced by the heavy Cd ions. Another contribution comes from the volume compaction of the SiO_2 matrix during the ion irradiation.^{12a} Annealing at 500 °C leads to a marked increase in thickness, by ca. 20%. Elevating the temperature to 700 °C does not change the layer thickness any more. At 800 °C a significant thickness loss, ca. 20%, is observed. The increase in volume upon annealing may be indicative of a continuing process of CdS formation initiated by implantation and the restoring of the SiO_2 network. Both cases rely on tetrahedral arrangements with directional bonding, resulting in open structures with large void volumes. The temperature for completing these processes seems to be ~ 500 °C, since no significant thickness change was observed at temperature above that level.

Nanometer-sized Cd particles are formed readily after the first step of Cd implantation (Figure 1a). A depth distribution in particle size covering a range from approximately 2 to 10 nm in diameter is apparent. The larger particles arrange slightly more toward the interface to Si_3N_4 . Such size distribution reflects qualitatively the concentration profile of Cd produced by implantation. The maximum Cd concentration is estimated¹³ to be at 51.8 nm from the surface. The additional implantation of S is visible in Figure 1b as a brighter outermost surface layer corresponding to a smaller ion range, ~ 21.9 nm,¹³ of S ions at 17 keV. The particles in this layer are seen to be growing in size with respect to the initial Cd particles. The inner layer is enriched in Cd. The two-layer feature of the implanted layer develops more clearly (Figure 1c) after a 500 °C annealing step. The outer layer increases in thickness and collects in it dominantly larger particles of uniform size and shape. Smaller particles are arranged in the inner layer. Furthermore, the implanted feature is observed to move away from the Si_3N_4 interface. This trend continues less markedly upon annealing at up to 700 °C (Figure 1d,e). The 800 °C annealing removes nearly completely the implanted features from the surface layer (Figure 1f).

More detailed information was obtained about the nanoparticles in terms of their phase identity, crystallinity, and morphology from HRTEM images, 1×10^6 magnification. Representative results are shown in Figure 2 for a sample annealed at 600 °C, indicating direct imaging of the lattice planes of the

nanoparticles. The crystallinity is evident by the individual lattice planes clearly visible in many particles. Results of lattice plane spacing measurements obtained from HRTEM images show that nanoparticles observed are crystalline CdS, CdO, and Cd laying randomly oriented in the matrix film. All samples implanted with Cd and S contain particles displaying lattice spacings of 3.4 and 3.6 Å. Both cubic ((100) planes) and hexagonal CdS ((002) planes) exhibit a 3.4 Å lattice spacing.^{15–17} The 3.6 Å value is consistent with the lattice spacing of the (100) planes of the hexagonal CdS phase.^{15,18–20} A corresponding distance for cubic CdS does not exist. Thus, the CdS phase observed in TEM is of hexagonal structure. In the Cd implanted sample the lattice spacings measured are 2.4 and 2.6 Å, which can be assigned to distances of the (101) and (100) planes of hexagonal Cd. The distance of 2.4 Å is also indicative of CdO seen in the (200) orientation (see below in XRD results). Cd is present also in samples additionally implanted with S, evidenced by the 2.8 Å spacing of (002) planes.

Bulk CdS, due to its ionic stabilization, exists only in a few crystalline structures. At ambient temperature and pressure, its thermodynamically stable phase is either of wurtzite (hexagonal) or zinc blende (cubic) structure, both being four-coordinate. All preparations performed at elevated temperatures, exceeding the kinetic barriers for phase transition, lead to the thermodynamically most stable structure wurtzite.^{21–24} A high level of the process temperature is the case in the present preparation. The observed hexagonal CdS phase is consistent with these general rules that its formation is thermodynamically controlled.

In the standard preparation routes the CdS phase formation is initiated by meeting of Cd^{2+} and S^{2-} ions with thermal energies that are molecular disperse and supplied mostly by diffusive processes. The implantation process under study produces in the first step Cd particles inside the SiO_2 matrix. Subsequently, S^+ ions are implanted into this surface layer. TEM images reveal Cd particles ~ 3 –8 nm in diameter. The ion range of 17 keV S^+ ions in Cd is theoretically estimated¹³ to be 21.9 ± 8.3 nm (longitudinal), which is larger than the Cd particle dimension. As a result, the Cd particles in the outermost layer will be resized upon collision with S^+ ions leading to intimate mixing to give CdS whereby a direct oxidation of Cd by S^+ ions may be the underlying chemistry of the sulfide formation. Evidence of this process is gained by comparing the TEM images of the Cd implanted sample and the (Cd + S) as-implanted sample (Figure 1). At greater depths, when losing sufficient energy, S^+ ions may be captured by Cd particles. Since understoichiometric S^+ ion doses (with respect to Cd^+) were applied, Cd particles in a deeper region from the surface may undergo reaction with S only partially. Particles with shell–core morphology are visible from some TEM images, suggesting a surface growing on preformed Cd particles.

Smaller particles appear spherical. The trend is evident that this shape is increasingly deformed toward prolate as the size becomes larger. The aspect ratio (ratio of the long to short dimension) measured from HRTEM images for larger particles reaches values of up to 1.4. The observed shape of the crystallites is the result of several interplaying affecting factors. By analogy with liquid droplets the observed spherical particles suggest a dominant contribution from surface energy (tension), since the equilibrium shape of a crystallite given by the Wulff's rule is nonspherical.

The dominant fraction of the crystallites is observed to possess an average diameter between 6 and 9 nm. The space restriction due to matrix presents one factor controlling the upper limit of the growing particles. The dimension of the cavities to

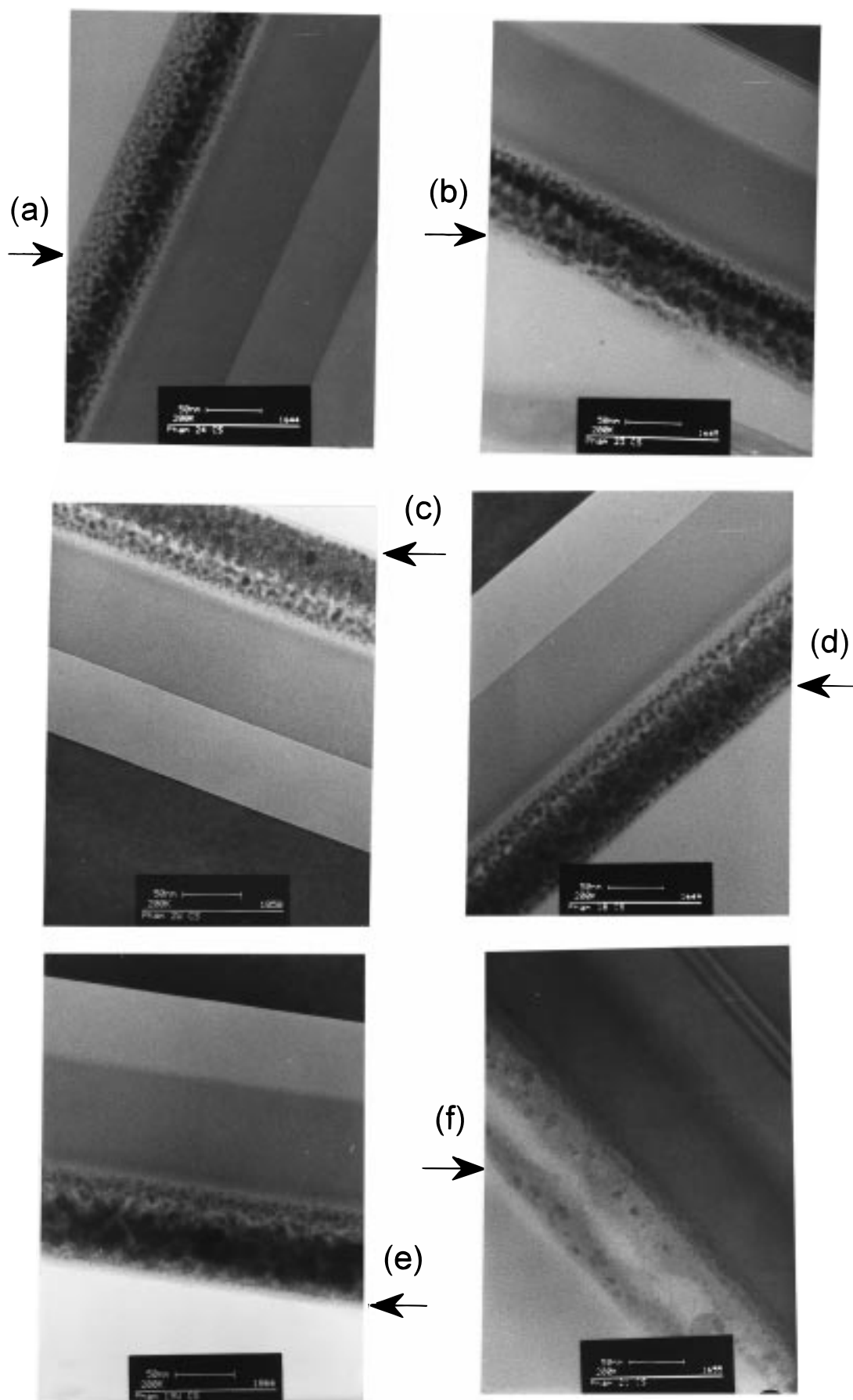
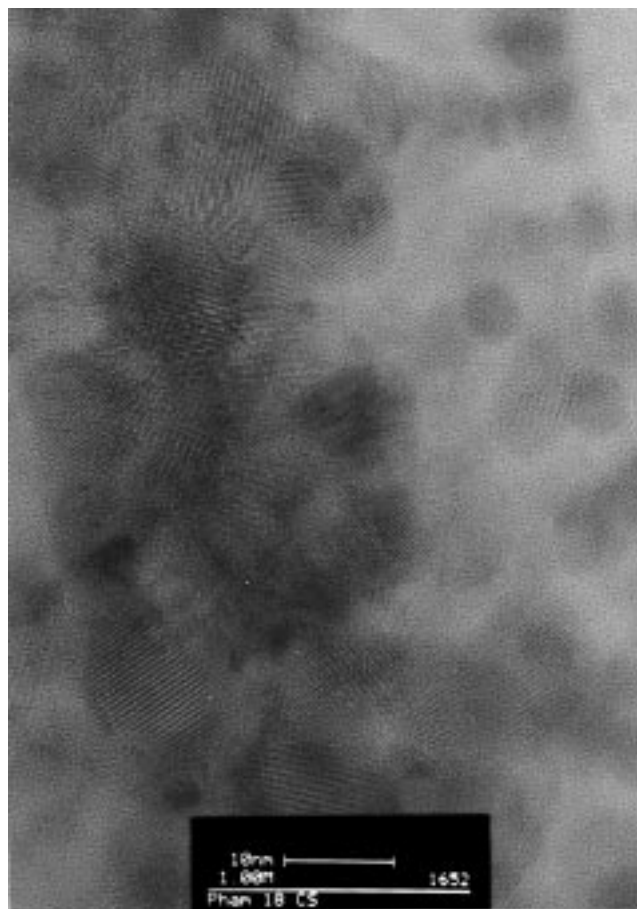


Figure 1. TEM images of the cross-sectional samples. The various stages of implantation and annealing are (a) Cd implantation, without annealing, (b) Cd and S implantation, without annealing, (c) like (b), 500 °C, (d) like (b), 600 °C, (e) like (b), 700 °C, (f) like (b), 800 °C. Arrows indicate surface positions.

TABLE 1: Thickness of the Implanted Layer

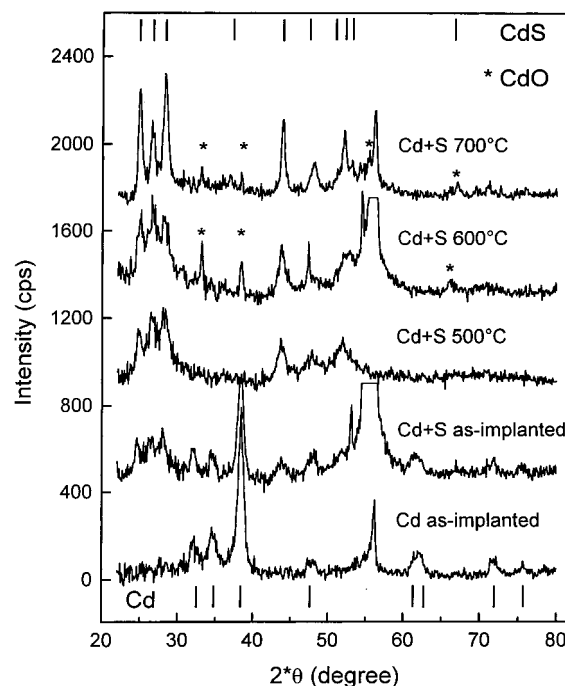
sample	thickness (nm)	sample	thickness (nm)
before impl	100	Cd + S, 600 °C	91
Cd as-impl	81	Cd + S, 700 °C	89
Cd + S as-impl	75	Cd + S, 800 °C	72
Cd + S, 500 °C	90		

**Figure 2.** HRTEM image revealing lattice planes of single CdS particles for a sample annealed at 600 °C.

accommodate the guest phase varies with the implantation conditions. Some extent of self-adjusting is achievable. Previous research has revealed the adjustability in the metrics and morphology of nanoscale metal particles by implantation parameters for some dielectric thin-film systems.^{12b} The preformed Cd particles are thought to give a controlling contribution to the CdS size. CdS is formed from both fractures of and intact Cd particles. The size range of CdS was seen to be comparable to that of Cd, suggesting this effect. A weak trend is observed in elevation in particle size for CdS compared to the case of Cd.

An evaluation of size distribution was not undertaken because of some uncertainty regarding the susceptibility of the material to electron beam during imaging. We observed for example material swelling and flowing. This fact is reflected in some of the TEM images presented in Figures 1 and 2. During the TEM sessions we could observe well discrete particles which then gradually aggregated with increasing exposure time.

Phase Composition. The phase composition of the implanted surface film was analyzed by XRD. Representative results are given in Figure 3 showing the XRD spectra for samples as-implanted and exposed to different annealing condi-

**Figure 3.** X-ray diffraction spectra of thin SiO₂ films implanted with Cd and S and exposed to different annealing temperatures for 10 min in nitrogen. From top to bottom: 700, 600, 500 °C, as-implanted, and Cd as-implanted sample. The positions of reflections for hexagonal CdS bulk, CdO, and Cd are indicated by small bars at the bottom.

tions. The spectra demonstrate clearly the formation and development of CdS in the SiO₂ film implanted with cadmium and sulfur.

All co-implanted samples reveal the diffraction peaks of the hexagonal greenockite modification of CdS (PDF-No: 41-1049²⁵). The positions of the CdS peaks are indicated by bars in the top of Figure 3. In the bottom the peak positions of pure cadmium (PDF-No: 5-674) are marked. Moreover, one observes some peaks from CdO in the montenopite modification (PDF-No: 5-640) indicated by an asterisk in Figure 3. The intense peak at 56° observed in some of the patterns results from scattering of the single crystalline substrate.

In the as-implanted state after the first step of Cd implantation one observes already diffraction peaks showing that the Cd is not randomly distributed in the matrix but has formed small crystals. After the second implantation step of S one observes both the diffraction peaks of Cd and of CdS. The formation of CdS is indeed induced during the implantation; nevertheless, the Cd diffraction peaks indicate the incompleteness of the phase formation. Therefore, unreacted S has to be assumed as well although not visible in the XRD results. Even if S crystallizes, the low symmetric structure makes an observation of diffraction peaks very unlikely because of the small sulfur amount. There are several factors that obviously are an obstacle to reaction completeness. The depth profiles of Cd and S are not exactly overlapping (see below). There is seemingly no stoichiometric quantities of Cd and S present in the implanted layer. Furthermore, S and Cd are involved actually in a heterogeneous reaction with energetic S atoms and Cd crystallites of finite size incorporated in the SiO₂ matrix.

Annealing of the samples at temperatures from 500 to 700 °C for 10 min enforces the CdS formation and with higher temperature a growth of crystallite size as seen from the three upper spectra in Figure 3. The reflections from Cd are absent in these patterns. The annealing at 500 and 600 °C effects mainly the full formation of CdS. With annealing temperatures

TABLE 2: Mean Crystallite Size Determined from the Bragg Reflections (100), (002), (101), (110), and (103) of CdS for Different Anneal Temperatures

	as-implanted	500 °C	600 °C	700 °C
size (nm)	7 ± 2	8 ± 0.8	8.5 ± 1.5	13 ± 3

as high as 700 °C grain growth is observed, the crystallites become larger and hence the diffraction lines sharper. Annealing at 800 °C destroys the CdS crystallites.

The determination of the growth mechanism of CdS from the diffraction data is difficult. The reduction of the crystallite size of Cd during S implantation (sample temperature 170 °C) may be caused by the propagation of the sulfiding toward Cd crystallite core and during annealing the process is completed. But the concurring process of CdS crystallite formation from dissolved atoms in the SiO₂ matrix also exists. This is evident since the grain growth of CdS at the 700 °C annealing is only possible by adding Cd and S atoms to the existing CdS crystallites.

The 600 and 700 °C the spectra (two upper curves in Figure 3) exhibit additionally diffraction reflections, more pronounced at 33° and 38°, consistent with a monteponite CdO phase. CdO appears diminished after 10 min at 700 °C (topmost spectrum) and completely disappears after 180 min at 700 °C (not shown in the figure). The trend observed fits reasonably to the enthalpy values for CdS and CdO (−162 and −258 kJ/mol²⁶) and the sublimation propensity of CdO starting at ca. 700 °C. The oxygen source for Cd oxidation came from the annealing ambient, since the matrix SiO₂ (−911 kJ/mol²⁶) is thermodynamically more stable than CdO. The increase in CdO diffraction intensity at 800 °C may arise from an increase in Cd concentration toward the surface from the bulk due to an enforced decomposition of CdS at this temperature. No more Cd reflection is observed in all the spectra for annealing temperatures above 500 °C, confirming furthermore that all Cd has previously been bound in CdS. CdS appears to persist up to 700 °C. Prolonged annealing, at 700 °C for 180 min, eliminates all implanted components Cd and S from the SiO₂ matrix.

The mean crystallite size was estimated from the line broadening of the most intense peaks by the Scherrer formula. The results are listed in Table 2. The average crystallite size of Cd in the as-implanted state after implantation of Cd alone was estimated to be 11 ± 1 nm. After the second implantation with S one observes a slight broadening of the Cd line width by about 10%, indicating a reduction in Cd crystallite size. The crystallite size for CdS coexisting with Cd is about 7 nm. This difference is too big to be explained with the sulfidization of Cd crystallites and the formation of a CdS shell around a Cd core as the dominating process. But it seems evident that part of the Cd atoms from the existing crystallites is involved in the CdS formation. The CdS diameters are seen to remain approximately constant (slightly increasing tendency) up to 600 °C. There is a jump on going from 600 to 700 °C. The loss of CdS due to decomposition and CdO formation is obviously one factor offsetting the CdS crystal growth observed in the temperature range below 700 °C. Another likely mechanism is due to the sulfiding of preformed and size-fixed Cd cores. The third affecting factor arises from the template effect of the matrix, restricting the crystal growth to hollows available within the matrix network. The mean size found in our case would correspond to a hollow diameter of ca. 10–12 nm for the SiO₂ matrix. The space restriction may account to some extent for the particle size being less sensitive toward a post-implantation annealing. The evaluation of the particle size from the peak

broadening is critical in some respects. The estimate obtained above gives nevertheless reasonable range and trends of the mean particle diameters consistent with the TEM results. The diffraction lines from CdS are quite weak, which is due to the small amount of material in the 100 nm SiO₂ film as well as the small crystallites. Nevertheless, one can judge that the intensity ratio between the peaks is in good correspondence with tabulated data²⁵ for bulk polycrystalline CdS. The latter is an expression for a nearly random orientation of the crystallites without texture effects. Although some shifts in peak position are observed during the annealing, the intensity ratios of the (100), (002), and (101) peak are not good enough for a detailed discussion.

Surface Chemistry. The XPS depth profile spectra are shown in Figure 4a for an as-implanted sample and in parts b and c of Figure 4 for annealed samples at 500 and at 800 °C, respectively. The depth profiles were taken at intervals of 2 min argon sputtering cycles. All data were corrected for electrostatic charging using the XPS lines of C 1s (on the surface) and Si 2p or O 1s (beneath the surface) as internal reference energy. The peak energy positions derived from the spectra are summarized in Table 3 for Cd 3d_{5/2}, S 2s, and O 1s. The corresponding standard values^{27–29} are given in parentheses. The results are representative for both surface and bulk, i.e., before and after sputtering. The S 2s photoemission lines for samples annealed at 500 and 800 °C display a peak at $E_B = 225.5(6)$ eV, consistent with the sulfide bond in CdS.^{30–32} The as-implanted sample shows a greater value of 226.7 eV, suggesting that some elemental S is also involved. The relative intensity decreases continually with increasing temperature, indicating changes in sulfide concentration with annealing. The Cd 3d_{5/2} peak positions appear at $E_B = 405.4(5)$ eV for all samples. These values are within the variation breadth of photoemission energies from CdS, CdO, and metallic Cd.^{27–29} Comparing with the Cd 3d_{5/2} spectrum (not shown here) of a sample without S implantation gives evidence that in the annealed samples Cd is involved predominantly in compounds, while metallic Cd is partially present before annealing. Oxygen is seen to be bound to silicon. Using the Si 2p energy position of 103.3 eV (corresponding to SiO₂) as energy reference, the oxygen 1s spectra reveal a peak position at $E_B = 532.6(7)$ eV independent of implantation and annealing. This value corresponds to the Si–O bonds in SiO₂ used as the matrix material. Since SiO₂ is present in excess, the expected O 1s emission line for CdO at $E_B = 529.2$ eV^{30–32} is not visible in the spectra.

Another notable feature is the annealing dependence of the spectrum shift due to electrostatic charging. Although the total amount of this spectral shift depends on the above-mentioned neutralizing effect of the electrons from the X-ray source, it is to be expected that the relative shifts are comparable, because the measuring conditions were quite similar. For the as-implanted sample the spectra are shifted to higher binding energy by 4.4 eV. Annealing at 500 °C alleviates apparently the level in spectrum shift, leading to a value of 2.3 eV. As the annealing temperature is elevated to 800 °C, an even higher value of 4.9 eV is observed. This behavior provides further evidence of CdS present in all samples prepared here. The electrostatic charging and its accompanying shift in XPS spectra are known to depend on the electrical conductivity of the surface film. For chemically deposited CdS thin films changes in conductivity and related shift in the XPS spectra upon annealing have been reported.^{30,33} The present result fits well to the phenomenon reported. The surface of the as-implanted sample is resistive due to CdS—the

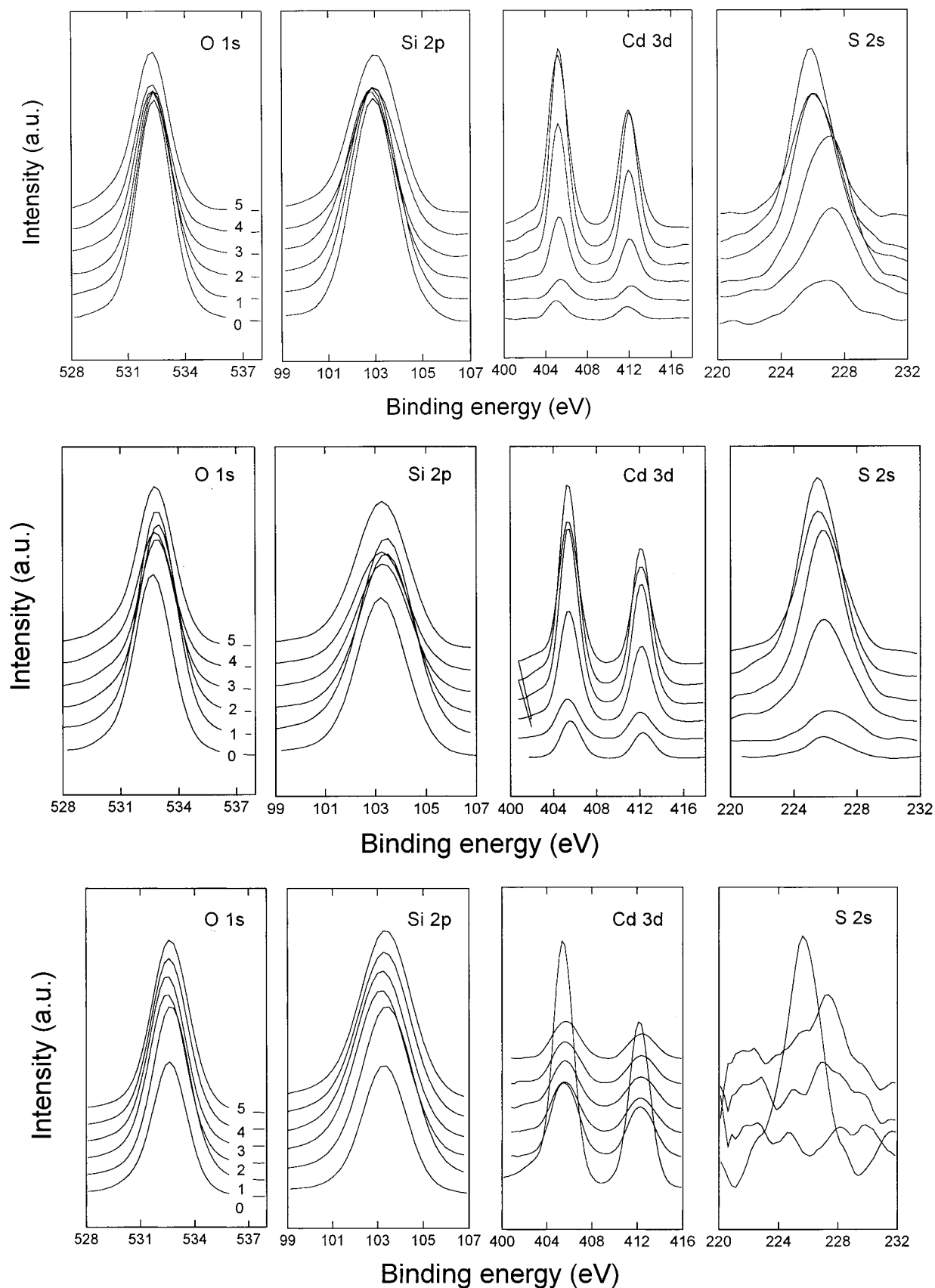


Figure 4. O 1s, Si 2p, Cd 3d, and S 2s XPS spectra of Cd and S implanted SiO_2 films for various sputter times (~ 3.6 nm/min): (a, top) as-implanted sample, (b, middle) 500 °C, and (c, bottom) 800 °C annealing for 10 min in nitrogen.

component governing the conductivity—being only partially formed. The 500 °C annealing seems to produce an increase in the CdS concentration and, more importantly, to convert to n-type CdS conductivity by Cd doping, thus leading to a marked

increase in conductivity of the sample surface. With the 800 °C annealing step the removal of CdS from the surface prevails, and the surface turns more resistive again tending toward that of the SiO_2 dielectric.

TABLE 3: Peak Energy Values for Cd 3d_{5/2}, S 2s, O 1s, and Peak Energy Difference Values for $\Delta 1 = E_{\text{Cd}} - E_{\text{S}}$, $\Delta 2 = E_{\text{O}} - E_{\text{Si}}$, and $\Delta 3 = E_{\text{O}} - E_{\text{Cd}}$, All in eV

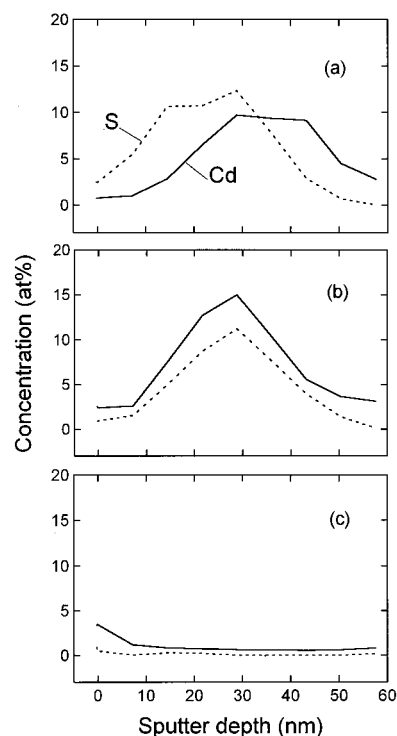
	Cd(405.3)	S(225.7)	O(532.7)	$\Delta 1(179.6)$	$\Delta 2(429.4)$	$\Delta 3(123.9)$
as-state	405.5	226.7	532.6	178.4	429.6	127.4
500 °C	405.5	225.5	532.6	179.9	429.2	126.4
800 °C	405.4	225.6	532.7	179.9	429.5	127.3

To support our assertion of the bonding states of Cd and S, we have analyzed additionally the differences (Δ) in peak energy between Cd 3d_{5/2} and S 2s, O 1s and Si 2p, and O 1s and Cd 3d_{5/2}. These values are free from charging effect. The results are listed in Table 3 with standard values given in parentheses.^{27–29} Again we find Cd and S bound in CdS and O bonded to SiO₂, as evidenced from the values $\Delta 1$ and $\Delta 2$. A smaller value $\Delta 1$ is observed for the as-prepared sample, signaling, in agreement with the discussion above, the presence of additional elemental sulfur. $\Delta 3$ deviates appreciably from that expected, indicating the undetectability of CdO under the experimental conditions considered here.

Figure 5 shows the sputter depth profiles obtained for an as-implanted sample (a), a 500 °C annealed (b), and a 800 °C annealed sample (c). The depth scale was obtained with a sputter rate of ca. 3.6 nm/min, as determined from the sputter time needed for the total implanted SiO₂ layer. The thickness of the latter was measured on a TEM image of a cross-sectional sample. Evident in Figure 5a is the nonoverlapping in Cd and S concentration, resulting in a distribution S-rich in the outer surface, Cd-rich in the bulk side, and nearly stoichiometric in the intermediate region. The maximum concentrations are at ~25 and ~40 nm for S and Cd, respectively, reflecting qualitatively the ion ranges estimated from TRIM¹³ for these implanted ions with 21.9 ± 8.3 and 51.8 ± 11.2 nm. However, the profile shape with plateau instead of maximum is less similar to an expected distribution. Although indicating the reaction of Cd and S toward CdS, the as-implantation results in a partial formation of CdS that is seen to arise from the nonoverlapping in depth profiles for the constituent reactants. The relatively low carbon content at the surface of the as-implanted sample is due to the residual ion sputtering during a former depth profiling experiment at another sample region. This fact shows, in addition, that the contamination layer is very thin.

Annealing leads to massive changes in the depth profiles. Both Cd and S are seen to be transported toward surface. A marked result of the 500 °C annealing is the redistribution to overlapping depth profiles for Cd and S. The important point is that the transport of Cd and S is not independent and is affected by the formation of CdS. Most evident is the Cd profile nearly perfectly copying that of the S profile, providing a clear signature of the reaction of Cd with S. This part of the profile corresponds thus to that of the CdS phase. This “CdS” profile appears very close to that defined by a S profile part on the bulk side and a Cd profile part on the surface side before annealing (Figure 5a). By taking account of some uncertainty in the profile determination, the conclusion appears reasonable that CdS is (i) readily formed during implantation, (ii) immovable upon annealing, and (iii) persistent at this temperature level. The obtained concentration in CdS is consistent with the sum of those formed before and after annealing.

The concentration of S was found to be exceptionally smaller than that of Cd, more pronouncedly even in the CdS region (Figure 5b), where the stoichiometry is expected. The atomic concentration ratio Cd/S is on average 1.5. One reason may be an artifact due to Ar sputtering. This phenomenon has been known for massive CdS thin films.³⁰ The dynamics of the

**Figure 5.** Sputter (~3.6 nm/min) depth profiles of Cd and S implanted in SiO₂ films: (a) as-implanted sample, (b) 500 °C, and (c) 800 °C annealing for 10 min in nitrogen.

sputtering process with Ar⁺ preferentially removes S and leads to a partial replacement of O for S in CdS according to CdS_{1-x}O_x. The abundance of oxygen from SiO₂ in our experiments favorably supports this mechanism. On the other hand, errors from the use of the standard elemental sensitivity factors²⁷ may occur.

There is a clear loss of Cd and S out of the surface upon annealing. S is seen to be removed more intensively than Cd. While S is readily depleted, Cd piles up markedly toward the surface. The difference is obviously related to the difference in sublimation and evaporation properties of these two elements. Only free (unreacted) Cd and S are observed to be movable. Figure 5b brings this point out most convincingly: the CdS profile (see above) is unaffected. The annealing at 800 °C (Figure 5c) destroys the CdS phase, leading to a nearly complete removal of all implanted components out of the surface. The annealing behavior observed reveals an important result. There is a temperature level below which a selective removal of unreacted Cd and S in favor of a CdS phase can be reached. This temperature seems to be at 500 °C or below where the CdS still persists whereas unbound Cd and S are readily movable.

To probe the chemistry in the outermost surface and to eliminate possible artifacts due to sputtering, XPS spectra were recorded by varying takeoff angles (relative to the sample surface). The variation range covers from 15° to 75°, corresponding to a maximum sampling depth of ca. 7 nm. The atomic compositions derived from these measurements are compiled in Table 4 for two marked steps of annealing at 500 and 800 °C compared with the case of the as-implanted state. The S 2p signal occurs in the running-out region of inelastic scattered Si 2s electrons and was identified only with some uncertainty. Results analyzed additionally for S 2s are therefore included. The line shapes for Cd 3d_{5/2}, S 2s, and O 1s confirm the results described before for the valence states of Cd and S as those in CdS, CdO, and elemental Cd and S. The results

TABLE 4: Variation of Chemical Composition (atom %) with Take-Off Angle

annealing	angle, deg	Cd 3d _{5/2}	S 2p	S 2s	O 1s	C 1s	Cd/S
as-state	15	0.17	0.32	0.32	36	44	0.5
	45	0.65	0.59	0.83	52	20	0.8
	75	1.06	1.3	1.3	56	14	0.8
500 °C	15	1.66	0.41	0.59	44	28	2.8
	45	1.40	0.02	0.2	62	10	7
	75	2.46	0.23	0.35	60	9	7.6
800 °C	20	3.86	1.3	1.6	44	23	2.4
	45	3.4	0.7	0.8	57	12	4.2
	75	3.26	0.4	0.7	57	10	4.7

are disturbed by a carbon contamination layer; therefore, only relative concentration values, last column in Table 4, may be relevant. The surface concentration's dependence on annealing qualitatively reproduces the trend observed for depth profiles seen above. S loses relative to Cd with increasing temperature. The trend of Cd and S to collect toward the surface is evident with increasing anneal temperature. Cd is enriched in the surface, the more the higher the temperature. This behavior is the result of (i) Cd and S are removed from the surface with different rates and (ii) the as-prepared state produces a surface composition with Cd in excess. The Cd/S ratio, rightmost column in Table 4, drops upon going from 500 to 800 °C annealing, supporting once again the immovable CdS phase at 500 °C. The 800 °C annealing supplies new free Cd and S by decomposing the CdS.

The possible chemistry of forming CdS consistent with the presented results appears to be the direct charge transfer from Cd to S⁺ ion. This reaction event is supported by the highly oxidizing power of the S⁺ ions, their directed impinging on the Cd reactant, and the high material density of the solid phase facilitating the energy dissipation. The observed elemental sulfur suggests further that a charge neutralization of S⁺ ions is also involved. A mixture of nonequilibrium reaction products is created due to the high quenching rate of the implantation process. This nonequilibrium is the driving force for the completion of the CdS formation achieved by the post-implantation annealing.

Conclusions

CdS nanocrystals immobilized inside thin films of SiO₂ can be prepared by implanting Cd⁺ and S⁺ ions into SiO₂ surface. This has been demonstrated for a 100 nm thin SiO₂ film of a multilayer structure SiO₂/Si₃N₄/SiO₂/Si with crystallites of CdS, nearly spherical in shape and of hexagonal structure, confined completely within the SiO₂ toplayer. The formation of CdS is the result of energetic S⁺ ions oxidizing preformed Cd nanoparticles. The reaction toward CdS is induced during implantation and completed by a subsequent annealing. Byproducts identified in the implanted layer are CdO and unreacted Cd and S. The thermal annealing leads to loss of Cd and S from the film and coarsening the CdS particles. There is an optimal temperature regime for removing the unreacted components Cd and S, which are less mobile relative to CdS, from the film. The film-immobilized nanocrystals are readily accessible to surface characterizing techniques.

Acknowledgment. This research was partially supported by the German Bundesministerium für Wirtschaft, Grant No. AiF-

9923B. The authors thank Dr. Schöneich and his team for their ion implantation work. The reviewers are gratefully acknowledged for their critical reading of the manuscript.

References and Notes

- (1) Murray, C. B.; Norris, D. J.; Bawendi, M. G. *J. Am. Chem. Soc.* **1993**, *115*, 8706.
- (2) Steigerwald, M. L.; Brus, L. E. *Acc. Chem. Res.* **1990**, *23*, 183.
- (3) Alivisatos, A. P. *J. Phys. Chem.* **1996**, *100*, 13226.
- (4) Henglein, A. *Chem. Rev.* **1989**, *89*, 1861.
- (5) Weller, H. *Angew. Chem., Int. Ed. Engl.* **1993**, *32*, 41.
- (6) Nirmal, M.; Murray, C. B.; Bawendi, M. G. *Phys. Rev. B* **1994**, *50*, 2293.
- (7) Danek, M. *Chem. Mater.* **1996**, *8*, 173.
- (8) Kagan, C. R. *Phys. Rev. Lett.* **1996**, *76*, 1517.
- (9) Mastai, Y.; Hodes, G. *J. Phys. Chem. B* **1997**, *101*, 2685.
- (10) (a) Colvin, V. L.; Goldstein, A. N.; Alivisatos, A. P. *J. Am. Chem. Soc.* **1992**, *114*, 5221. (b) Bowen Katari, J. E.; Colvin, V. L.; Alivisatos, A. P. *J. Phys. Chem.* **1994**, *98*, 4109.
- (11) Ekimov, A.; Gurevich, S.; Kudriavtsev, I.; Lublinskaya, O.; Merkulov, A.; Osinskii, A.; Vatnik, M.; Grandais, M.; Wang, Y. *J. Cryst. Growth* **1995**, *151*, 38.
- (12) (a) Townsend, P. D.; Chandler, P. J.; Zhang, L. *Optical Effects of Ion Implantation*; Cambridge University Press: New York, 1994. (b) Pham, M. T.; Matz, W.; Seifarth, H. *Anal. Chim. Acta* **1997**, *350*, 209. (c) Pham, M. T.; Möller, D.; Hüller, J.; Albrecht, J. *J. Appl. Phys.* **1996**, *79*, 3915.
- (13) Ziegler, J. F.; Biersack, J. P.; Littmark, U. *The Stopping and Range of Ions in Solids*; Pergamon: New York, 1985; Vol. 1.
- (14) Armini, A. J.; Bunker, S. N. *Sci. Eng., A* **1989**, *114*, 67.
- (15) Vossmeier, T.; Katsikas, L.; Giersig, M.; Popovic, I. G.; Diesner, K.; Chemseddine, A.; Eychemüller, A.; Weller, H. *J. Phys. Chem.* **1994**, *98*, 7665.
- (16) Korgel, B. A.; Monbouquette, H. G. *J. Phys. Chem.* **1996**, *100*, 346.
- (17) (a) Pamplin, B. R.; Berger, L. I. *CRC Handbook of Chemistry and Physics*; CRC Press: Boca Raton, FL, 1990. (b) West, A. R. *Solid State Chemistry and Its Applications*; John Wiley and Sons: New York, 1984.
- (18) Spanhel, L.; Haase, M.; Weller, H.; Henglein, A. *J. Am. Chem. Soc.* **1987**, *109*, 5649.
- (19) (a) Routkevitch, D.; Bigioni, T.; Moskovits, M.; Xu, J. M. *J. Phys. Chem.* **1996**, *100*, 14037. (b) Klein, J. D.; Herrick, R. D., II; Palmer, D.; Sailor, M. J. *Chem. Mater.* **1993**, *5*, 902.
- (20) Rockenberger, J.; Tröger, L.; Kornowski, A.; Vossmeier, T.; Eychemüller, A.; Feldhaus, J.; Weller, H. *J. Phys. Chem. B* **1997**, *101*, 2691.
- (21) Haase, M.; Alivisatos, A. P. *J. Phys. Chem.* **1992**, *96*, 6756.
- (22) Chen, C. C.; Herhold, A. B.; Johnson, C. S.; Alivisatos, A. P. *Science* **1997**, *276*, 398.
- (23) Tolbert, S. H.; Alivisatos, A. P. *Annu. Rev. Phys. Chem.* **1995**, *46*, 595.
- (24) Fitzpatrick, B. J. In *Growth and Optical Properties of Wide-Gap II–VI Low-Dimensional Semiconductors*; McGill, T. C., Torres, C. M. S., Gebhardt, W., Eds.; Plenum: New York, 1989; p 67.
- (25) The powder diffraction file, set 1–46, International Centre for Diffraction Data, Newtown Square, PA 19073-3273.
- (26) Lide, D. R., Ed. *Handbook of Chemistry and Physics*; CRC Press: Boca Raton, FL, 1994.
- (27) Christian, J., Ed. *Handbook of Photoelectron Spectroscopy*; Physical Electronics: Eden Prairie, 1992.
- (28) Briggs, D.; Seah, M. P., Eds. *Practical Surface Analysis*; John Wiley & Sons: New York, 1990; Vol. 1.
- (29) Wagner, C. D.; Riggs, W. M.; Davis, L. E.; Moulder, T. F.; Muilenberg, G. E. *Handbook of X-ray Photoelectron Spectroscopy*; Perkin-Elmer: Norwalk, CT, 1978.
- (30) Niles, D. W.; Herdt, G.; Al-Jassim, M. J. *Appl. Phys.* **1997**, *81*, 1978.
- (31) Nair, M. T. S.; Nair, P. K.; Zingaro, R. A.; Meyers, E. A. *J. Appl. Phys.* **1994**, *75*, 1557.
- (32) Hashimoto, Y.; Nakanishi, T.; Andoh, T.; Ito, K. *Jpn. J. Appl. Phys.* **1995**, *34*, L382.
- (33) Kohle, S.; Kulkarni, S. K.; Nijaveka, A. S.; Sharma, S. K. *Sol. Energy Mater.* **1987**, *10*, 47.